Chemical Science

EDGE ARTICLE

Check for updates

Resolving the ultrafast dynamics of the anionic green fluorescent protein chromophore in water†

Chey M. Jones, [ab] Nanna H. List [ab] and Todd J. Martínez *[ab]

The chromophore of the green fluorescent protein (GFP) is critical for probing environmental influences on fluorescent protein behavior. Using the aqueous system as a bridge between the unconfined vacuum system and a constricting protein scaffold, we investigate the steric and electronic effects of the environment on the photodynamical behavior of the chromophore. Specifically, we apply *ab initio* multiple spawning to simulate five picoseconds of nonadiabatic dynamics after photoexcitation, resolving the excited-state pathways responsible for internal conversion in the aqueous chromophore. We identify an ultrafast pathway that proceeds through a short-lived (sub-picosecond) imidazolinone-twisted (I-twisted) species and a slower (several picoseconds) channel that proceeds through a long-lived phenolate-twisted (P-twisted) intermediate. The molecule navigates the non-equilibrium energy landscape *via* an aborted hula-twist-like motion toward the one-bond-flip dominated conical intersection seams, as opposed to following the pure one-bond-flip paths proposed by the excited-state equilibrium picture. We interpret our simulations in the context of time-resolved fluorescence experiments, which use short- and long-time components to describe the fluorescence decay of the aqueous GFP chromophore. Our results suggest that the longer time component is caused by an energetically uphill approach to the P-twisted intersection seam rather than an excited-state barrier to reach the twisted intramolecular charge-transfer species. Irrespective of the location of the nonadiabatic population events, the twisted intersection seams are inefficient at facilitating isomerization in aqueous solution. The disordered and homogeneous nature of the aqueous solvent environment facilitates non-selective stabilization with respect to I- and P-twisted species, offering an important foundation for understanding the consequences of selective stabilization in heterogeneous and rigid protein environments.

Introduction

Since their initial characterization in *Aequorea victoria*,[1–5] fluorescent proteins (FPs) have emerged as powerful probes for *in vivo* biological function.[6–11] The green fluorescent protein[8] (GFP) is the monarch of FPs, and its utility and versatility keep the green fluorophore at the forefront of science. Seminal experiments on the color and protonation state tuning of GFP[12–17] inspired novel FP biomarkers, with reversible photoswitchable FPs propelling image resolution beyond the diffraction limit.[16–18] Located at the heart of GFP, a tunable chromophore is responsible for GFP's light emission. Because the native characteristics of GFP can be altered significantly by applying point mutations near the site of the chromophore,[8] we need a detailed understanding of the chromophore's local steric and electronic

environment to optimize the versatility of GFP. Frequently, *p*-hydroxybenzylidene-2,3-dimethylimidazolinone (HBDI), first synthesized by Kojima *et al.*,[19] serves as a model GFP chromophore. In particular, the anionic form of HBDI (HBDI⁻) mimics the protonation state of the chromophore responsible for fluorescence in the protein.[20,21]

The overwhelming number of variables in a complex protein environment creates a fundamental roadblock to the rational design of FPs. Due to the rigidity of its 11-stranded β-barrel,[22,23] GFP envelops its chromophore in a highly ordered pocket of amino acids. Stiff protein backbones foster heterogeneous electronic and steric fingerprints that can significantly impact the chromophore's behavior.[8] Because amino acids in GFP form complex networks of covalent and non-covalent interactions, it is difficult to predict the net effect of various residues acting on the chromophore. To filter out the effects that dictate chromophore behavior, we use HBDI⁻ to monitor the molecule's response to incremental perturbations of the environment. Using the gas-phase dynamics of HBDI⁻ as a baseline,[24] we identify the influence of steric and electronic effects on

ᵃDepartment of Chemistry and the PULSE Institute, Stanford University, Stanford, CA 94305, USA. E-mail: toddjmartinez@gmail.com

ᵇSLAC National Accelerator Laboratory, 2575 Sand Hill Road, Menlo Park, CA 94025, USA

chromophore behavior in solution, focusing on the homogeneous and disordered case of aqueous HBDI⁻.

Solvated HBDI⁻ straddles the line between the freedom permitted by the gas-phase and the confinement imposed by a protein. In water, HBDI⁻ experiences steric and electronic effects from the solvent, which are absent *in vacuo*, while in an environment that is less constricting than a protein scaffold. Time-resolved spectroscopies reveal that GFP has an excited-state lifetime on the order of nanoseconds[20,25,26] and a fluorescence quantum yield near unity.[8] Yet, HBDI⁻ experiences ultrafast internal conversion in vacuum and in solution at ambient temperature.[27–31] Twisting around the bridge bonds connecting the imidazolinone (I) and phenolate (P) moieties of the isolated chromophore leads to ultrafast deactivation that decreases fluorescence quantum yield.[31–33] As highlighted in previous computational studies,[34,35] non-methylated HBDI⁻ (pHBI⁻) undergoes twisted intramolecular charge-transfer (TICT) as rotations of the I- and P-moieties become sufficiently large. The direction of charge-transfer (CT) on the excited state depends on whether rotation occurs along the I- or P-dihedral (ϕ_I/ϕ_P dihedrals illustrated in Fig. 1, respectively). Whereas rotation of ϕ_I induces CT from the I-ring to the P-ring in the gas-phase, rotation of ϕ_P induces CT from the P-ring to the I-ring.

Using ultrafast fluorescence and polarization spectroscopy experiments,[27,36,37] Meech and co-workers identified similar short (hundreds of femtoseconds) and long (picoseconds) decay components for HBDI⁻ across a variety of solvents. In water, time constants of 210 fs and 1.1 ps were reported for fluorescence decay—significantly faster than the 1.3/11.5 ps excited-state lifetimes reported *in vacuo*.[21,30] Early quantum chemical calculations on gas-phase pHBI⁻[38] suggested that a volume-conserving "hula-twist" deactivation mechanism[39,40] is

responsible for the limited sensitivity of the chromophore's excited-state lifetime on solvent viscosity. However, more recent calculations implicate drastic torsional motion along either of the methine bridge bonds as responsible for the ultrafast deactivation of the anionic chromophore.[34,41] This behavior is corroborated by high-level quantum mechanics/molecular mechanics (QM/MM) simulations in water using extended multistate multireference second-order perturbation theory (XMS-CASPT2)[42] and spin-flip time-dependent density functional theory.[43] These studies found that the dominant decay pathway of pHBI⁻ is through the I-twisted channel. However, the limited simulation time considered (1 ps) did not allow identification of the sources responsible for the multi-timescale decay in solution. To resolve this, we simulate multiple picoseconds of the aqueous HBDI⁻ photodynamics while monitoring important geometric and electronic features of the system.

Ultrafast dispersed pump-dump-probe experiments of HBDI⁻ in water present excited-state decay lifetimes in the 620–940 fs range for twisted excited-state intermediates.[44] Although the imperfect selectivity of a dump pulse may make it difficult to attribute time constants to specific processes, the Z/E isomerization quantum yield derived from these experiments was below the detection threshold of ∼5%. Solution-phase studies on the chromophore's protonated counterpart, HBDI, demonstrate that the solvent can have a noticeable impact on isomerization quantum yield.[45,46] In aprotic solvents, HBDI recorded Z/E photoisomerization quantum yields of ∼50%. This yield drops to ∼10–20% in protic solvents, where excited-state proton transfer is a competing process. While torsion along ϕ_I can result in the E-isomer (Z/E isomerization), torsion along ϕ_P will regenerate the Z-isomer due to the symmetry of the P-ring (Z/Z isomerization). Thus, Z/Z isomerization products are experimentally indistinguishable from decay pathways that do not involve isomerization. For this reason, it remains unclear what ratio of excited-state species proceeds toward photoproduct formation (Z/E isomerization), undergoes P-ring flip (Z/Z isomerization), or re-populates the original ground state (Z-isomer).

A key ingredient of QM/MM (or fully QM) simulations of photochemistry is the proper description of the potential energy surface topography around conical intersections (CIs). Many electronic structure methods are not capable of correctly describing S_0/S_1 CI regions[47–49] (*e.g.* time-dependent density functional theory and other single-reference methods). Following our recent gas-phase study,[24] we use the α-CASSCF method,[50] which provides a correct and efficient description of the exact degeneracy and relative energetics along key deactivation coordinates. This enables us to extend our simulations to multiple picoseconds. Consequently, we are able to monitor the chromophore's approach toward the CI seams and provide predictions for the photoproduct branching. The shape of CIs (*e.g.* peaked *vs.* sloped) can also be critically important in determining the photoproducts.[51–54] Although it appears that the CIs become more peaked upon solvation for the neutral GFP chromophore[55,56] (suggesting a shortening of the excited-state lifetime and a larger isomerization quantum yield), the shape
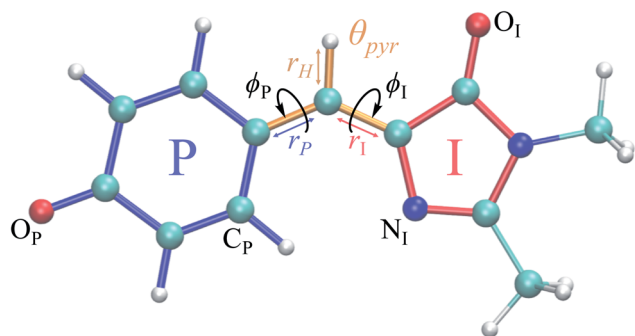

Fig. 1 Structure of the HBDI⁻ model chromophore illustrating key geometric parameters. Cyan atoms represent carbon, red atoms represent oxygen, blue atoms represent nitrogen, and white atoms represent hydrogen. Blue, red, and orange bonds connect atoms belonging to the P-ring, I-ring, and methine bridge, respectively. ϕ_I is defined as the dihedral angle formed by N_I and the carbon atoms of the methine bridge. ϕ_P is defined as the dihedral angle formed by the carbon atoms of the methine bridge and C_P. The pyramidalization of the central methine carbon atom, θ_{pyr}, is calculated as $\cos^{-1}((\vec{r}_P \times \vec{r}_I) \cdot \vec{r}_H) - \pi/2$ and uses the bridge bond vectors in a method similar to Radhakrishnan *et al.*[71] For reference, the pyramidalization angles of ideal sp^2 and sp^3 hybridized carbon atoms using this definition are 0° and 55°, respectively.

of the CIs that govern nonadiabatic transitions for HBDI$^-$ in water has been largely unexplored.

Recent femtosecond stimulated Raman spectroscopy (FSRS) and transient absorption experiments of aqueous HBDI^{-31} fill in some of the gaps left by ultrafast fluorescence experiments. While time-resolved fluorescence experiments elucidate the temporal signatures of highly fluorescent HBDI$^-$ species, i.e., closer to the Franck–Condon (FC) point, FSRS is able to track the progression of HBDI$^-$ along vibrational modes of dark, non-fluorescent species. FSRS studies yield three time constants for the excited-state dynamics of HBDI$^-$: ~350 fs, 2–3 ps, and ~250 ps.[31] These were tentatively assigned to the formation of a charge-separated (CS) species, the transition from the CS state to a TICT state, and ground-state recovery of the Z-isomer, respectively.

In this work, we explore the internal conversion dynamics following photoexcitation of explicitly-solvated HBDI$^-$. Using ab initio multiple spawning[57–61] (AIMS), we provide insight into the primary deactivation pathways in aqueous solution and each pathway's relative accessibility to CIs. In particular, we investigate the characteristics of HBDI$^-$ (i) at the FC region, (ii) out of the FC region as the molecule approaches CI seams, (iii) upon encountering the CI seam, and (iv) away from the CI seam as it returns to the ground state. This non-equilibrium picture (chromophore and solvent response) is compared to the corresponding excited-state equilibrium solvation picture, defined by the free energy surface of aqueous HBDI$^-$. Our results are interpreted in the context of previous experiments performed in silico, in vacuo, and in solution. Using this approach, we discuss the impact of solvation on HBDI$^-$ and develop a more complete picture of GFP chromophore photophysics.

Computational details and methods

Because of its efficiency and ability to describe CIs, state-averaged[62] complete active space self-consistent field (SA-CASSCF)[63–65] was chosen as the electronic structure method for HBDI$^-$ in water. To increase the accuracy of SA-CASSCF, we correct for the lack of dynamic electron correlation in SA-CASSCF calculations by using α-CASSCF[50] (Fig. S1†). The α-CASSCF method uses energy scaling to approximate the effects of dynamic electron correlation at the cost of traditional SA-CASSCF,[66] similar to previous scaling methods introduced by Olivucci and coworkers.[67] Orbitals are optimized to minimize the average energy of the three lowest singlet electronic states in SA-CASSCF, as this has been shown to provide an accurate excited-state description of I- and P-torsional pathways.[68] In particular, inclusion of three states captures the P-twisted minimum energy conical intersection (MECI) of HBDI$^-$, which can be elusive when using a two-state averaging method with CASSCF.[69] An active space of four electrons in three orbitals, i.e., SA3-CASSCF(4,3), incorporates the bonding, non-bonding and anti-bonding π-orbitals relevant to describe the allylic anionic character of the methine bridge (Fig. 2). Unless stated otherwise, the 6-31G* basis set[70] is used throughout.

The α parameter was chosen to reproduce the S$_0$ → S$_1$ vertical excitation energy of the planar chromophore in
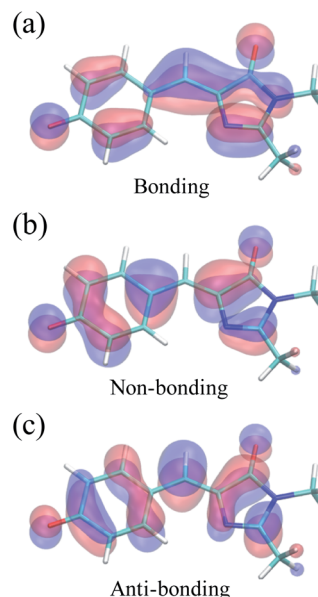

Fig. 2 Active space orbitals of HBDI$^-$ from α(0.67)-SA3-CASSCF(4,3) at the FC point: the anionic, allylic (a) bonding, (b) non-bonding, and (c) anti-bonding orbitals.

solution, computed with the SA3-XMS-CASPT2(4,3) method[72–74] (1s orbitals of heavy atoms were excluded from the perturbation treatment and a level shift of 0.3 a. u. was used). This led to an α value of 0.67 for hydrated HBDI$^-$ (Fig. S1†). This is very similar to the α value of 0.64 which we found for isolated HBDI$^-$ (used in the gas-phase calculations reported herein).[24] As shown in Fig. S1,† this α-CASSCF method reproduces XMS-CASPT2 potential energy profiles along the two bridge torsional coordinates (ϕ_I and ϕ_P). Unless otherwise stated, all calculations were performed with α(0.67)-SA3-CASSCF(4,3)/6-31G* in explicit solvent. Relative energies, geometric parameters, and transition dipole moments of representative optimized geometries are provided in the ESI† (Fig. S1–S3 and Tables S1–S4). Fractional occupation number Hartree–Fock (FON–HF) was used to determine initial guess orbitals for the α-CASSCF calculations (using Gaussian broadening with an electronic temperature of 0.3 a. u.).[75–78]

Critical points were obtained using the DL-FIND geometry optimization library.[79] Electronic structure calculations were performed with TeraChem.[80–84]

Solvated initial conditions

A Boltzmann sampling procedure provided initial conditions (ICs) for the solvated chromophore. Using PACKMOL,[85] HBDI$^-$ was immersed in a solvent sphere comprised of 2000 water molecules and a sodium counterion. The radius of the solvation sphere was 24.3 Å, consistent with the density of liquid water (0.997 g mL^{-1}). Classical dynamics were run with OpenMM,[86] and a restraining spherical force of 10 kcal mol^{-1} Å^{-2} was applied to the water sphere during the dynamics. The solvent was equilibrated by performing a 5 ns NVT classical dynamics simulation, using a Langevin thermostat at 300 K, with the

geometry of the chromophore fixed. Water molecules were treated with the flexible SPC/Fw model,[87] and the sodium ion was modelled using van der Waals parameters previously determined for use in SPC/E water.[88] Atomic charges for the chromophore were fit using the restrained electrostatic potential[89] procedure with HF/6-31G*, based on the B3LYP-D3/6-31G** optimized geometry of the chromophore in the gas-phase.[90–92] Van der Waals parameters for the chromophore were taken from the general Amber force field.[93] Other force field parameters (such as equilibrium bond lengths/angles and associated force constants) are irrelevant because the chromophore was kept fixed during the MM simulations used to relax the solvent environment.

Following the initial solvent equilibration, the geometric constraints on the chromophore were lifted and a 10 ps ground-state QM/MM molecular dynamics (QM/MM-MD) trajectory, within the NVT ensemble, was run to obtain ICs for the nonadiabatic dynamics simulations. The chromophore was treated at the QM level (described above), whereas the waters and sodium ion were treated at the MM level. A D3 dispersion correction was included for the QM region, using Hartree–Fock parameters.[92] Spherical boundary conditions were again employed to avoid evaporation of water molecules. QM/MM-MD simulations were performed with a Langevin thermostat at 300 K, using the time-reversible Niklasson integrator[94] and a time step of 0.5 fs. After an equilibration period of 3 ps, a total of 500 temporally-equidistant samples were extracted from the remaining 7 ps of QM/MM-MD to generate an absorption spectrum. The stick spectra were convolved with a Gaussian lineshape function, using a full width at half maximum (FWHM) of 0.40 eV based on solution-phase experiments.[95]

Nonadiabatic dynamics

A total of 50 ICs were extracted from the 500 QM/MM-MD samples (every tenth IC) and used to initiate AIMS simulations within the independent first generation approximation.[60,61] Using this sampling procedure, we minimize the correlation between ICs. Moreover, this sampling procedure enables us to partition ICs based on their location in the aqueous HBDI$^-$ absorption spectrum, which is necessary to investigate the wavelength dependence of excited-state deactivation. ICs are classified as either red-shifted or blue-shifted based on their excitation energy relative to the computed absorption maximum (computed as 2.84 eV, compared to the measured value of 2.91 eV (ref. 31 and 95)). When comparing our simulations to experiment, it should be noted that the wavelength of the pump used in previous time-resolved spectroscopy experiments[31,96] was on the blue-edge of the spectrum (400 nm, $i.e.$, 0.2 eV blue-shifted from the absorption maximum). The AIMS simulations were continued for 5 ps or until at least 99% of the excited-state population for a given initial trajectory basis function (TBF) was transferred to the ground state. If a TBF on S_0 went at least 5 fs without coupling with another TBF (as measured by the TBF overlap, with a threshold of 0.6), the TBF on S_0 was removed from the set of coupled TBFs and run independently for the remainder of the

simulation. The threshold for spawning (based on the dot product of the nonadiabatic coupling vector and the velocity) was defined as 0.005 a.u. The spherical boundary conditions applied for QM/MM-MD were employed during the AIMS dynamics as well. Error bars for exponential fitting of the S_1 population were obtained using a bootstrapping method[97] that included 1000 bootstrapping samples. To gauge the branching ratio of photoproducts from AIMS dynamics, each spawned TBF on S_0 was propagated independently for an additional 500 fs. By the end of the extended ground-state dynamics, the TBFs were classified based on the ϕ_I and ϕ_P values of their S_0 nuclear configuration. If the magnitude of either dihedral was above 120°, the product was classified as isomerized with respect to that angle. The resulting photoproducts were used to quantify photoisomerization quantum yield. Geometric analysis of AIMS trajectories was aided by MDTraj.[98]

Umbrella sampling

To provide insight regarding the free energy landscape and entropic effects of HBDI$^-$ in water, QM/MM umbrella sampling at 300 K was performed on S_1. A two-dimensional mapping was performed along the ϕ_I and ϕ_P twisting coordinates (ranging from −120° to 120°, using 10° intervals for a total of 625 sampling windows). To compensate for incomplete sampling of solvent configurations, we augmented the data to incorporate the symmetry with respect to twisting of the ϕ_I and ϕ_P dihedral angles (Fig. S4†). Specifically, each data point ($i.e.$, energy, oscillator strength) for an observed geometry contributed to two data points: one for the observed geometry and one for its enantiomer, where $\phi_{\text{enantiomer}} = -\phi_{\text{observed}}$ for both ϕ_I and ϕ_P. Convergence analysis of the two-dimensional free energy surface indicated that an equilibration time of 1.5 ps for each window provided a sufficient compromise between sampling and computational cost (Fig. S5†). After the equilibration, 2 ps of data was collected for each window to generate the potential of mean force[99] (PMF). In total, over 2 ns of excited-state QM/MM-MD simulations were run to obtain the free energy surface. A harmonic biasing potential with a force constant of 100 kcal mol^{-1} Å^{-2} was applied to both dihedrals. Contour plots were generated using a cubic interpolation between points on the free energy grid obtained from unbiasing a set of biased sampling windows via the weighted histogram analysis method.[100,101]

Time-resolved fluorescence

Two-dimensional fluorescence spectra of HBDI$^-$ were generated based on the AIMS simulations. Spectra were obtained as:

$$F(t, \nu) \propto \sum_{I \in S_1}^{N_{\text{TBFs}}} n_I(t) \left| \mu_{S_0/S_1} \left(\overline{R}_I(t) \right) \right|^2$$

$$\left(\frac{\Delta E_{S_0/S_1} \left(\overline{R}_I(t) \right)}{h} \right)^3 \delta \left(\Delta E_{S_0/S_1} \left(\overline{R}_I(t) \right) - h\nu \right) \quad (1)$$

where the sum is restricted to TBFs that are propagating on S_1, h is Planck's constant, $n_I(t)$ is the S_1 population of the Ith TBF,

$\mu_{S_0/S_1}(R)$ is the transition dipole moment between S_0 and S_1 at molecular geometry R, $\Delta E_{S_0/S_1}(\bar{R}_I)$ represents the S_0/S_1 energy gap, and $\bar{R}_I(t)$ is the position centroid of the Ith TBF at time t.[102] The time-resolved fluorescence spectra were convolved with a Gaussian having FWHM of 0.15 eV in the energy domain (ν) and 100 fs in the temporal domain (t) to simulate the instrument response function of previous fluorescence up-conversion experiments.[27,103] For each two-dimensional fluorescence spectrum, the energy was shifted by 0.13 eV to align the fluorescence intensity maxima obtained from theory and experiment (*vide infra*).[31] Once shifted, the decay signal corresponding to an intensity slice at 500 nm was extracted and analyzed to elucidate the fluorescence behavior of HBDI$^-$ over the course of the dynamics.

Results and discussion

To begin describing the effects of solvation, we observe how the absorption spectrum of HBDI$^-$ changes when the molecule is immersed in water. Fig. 3a compares the simulated and experimental absorption spectra of HBDI$^-$ in vacuum[24] and aqueous solution. Solvation of HBDI$^-$ blue-shifts the absorption maximum (0.41 eV), as is also observed in experiment (0.32 eV).[31,95,104] As summarized in Table S5,† the electronic properties of water are primarily responsible for blue-shifting the absorption maximum of HBDI$^-$ upon solvation (0.19 eV), whereas the geometric changes have a minimal contribution (0.03 eV) to the spectral shift. Radial distribution functions (RDFs), based on the ground-state QM/MM-MD, between water oxygen atoms and the heteroatoms in HBDI$^-$ provide a description of local solvation. As shown in Fig. 3b, the RDF for the O_P atom indicates that it is more tightly coordinated to water than the O_I atom. This is consistent with the enhanced charge localization on O_P, relative to O_I, in the ground state (see Fig. S6† for fragment-accumulated Mulliken charges).

To understand the limited impact of geometric perturbations, we analyze the initial distribution of key geometric parameters to observe how the sampled configuration space changes upon solvation. Fig. 4a shows the bond length distributions for the bridge bonds, r_I and r_P, from the ground-state QM/MM-MD. In water, the bridge bonds of HBDI$^-$ sample a narrower region of configuration space when compared to vacuum. This difference is related to whether a quantum or classical sampling technique is used, as indicated by the similar configuration space sampled by gas-phase and solution-phase HBDI$^-$ using QM/MM-MD sampling in both instances (Fig. S7†). Distributions for the solvated ICs used for the AIMS dynamics are shown in Fig. S8.† The average r_I-to-r_P bond length ratio in water is consistent with a stabilization of the phenolate resonance structure, in line with the RDFs in Fig. 3b. Therefore, we verify that the phenolate resonance structure of HBDI$^-$ is favored throughout the ground-state dynamics in water, as suggested by calculations in a polarizable continuum water model.[41] While the phenolate and quinoid resonance structures contribute almost equally in gas-phase,[24,68] the decrease in the r_I-to-r_P ratio upon solvation indicates a preference toward the phenolate resonance structure in solution. Interestingly, the distributions along the ϕ_I and ϕ_P dihedrals (Fig. 4b) remain almost identical between systems. The striking similarity between these angular distributions indicates that the presence of mobile water molecules does not restrict the chromophore's motion along its twisting dihedrals on the ground state. The concerted rotation around the I- and P-bonds, which are connected by the methine bridge carbon atom and adjacent to one another, is reminiscent of hula-twist motion.[39,40] However, we observe conrotatory rotation of ϕ_I and ϕ_P, as opposed to the volume-conserving disrotatory motion.[105]

Electronic effects of equilibrium solvation

Before investigating the photodynamics of HBDI$^-$, we consider the excited-state landscape in the equilibrium solvation regime.
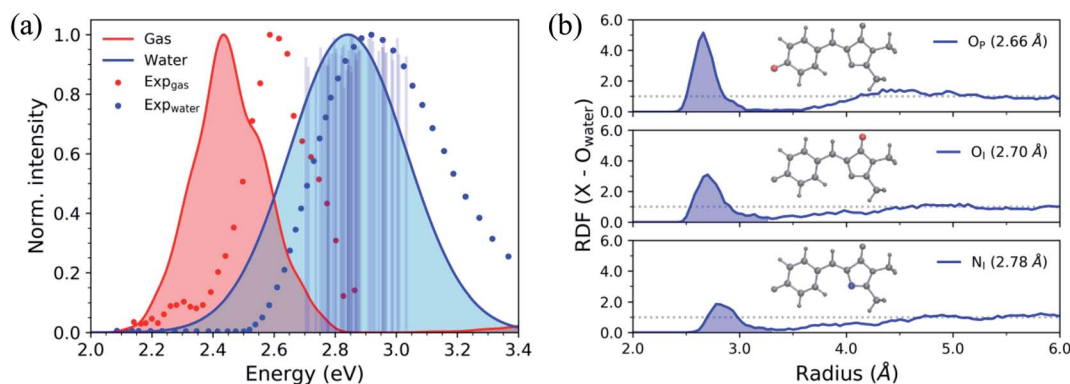
Fig. 3 (a) Simulated absorption spectra of HBDI$^-$ in gas-phase (red) and water (blue) using 500 ICs from each system. Sticks represent the S_0/S_1 excitation energy and their relative oscillator strengths for the 50 solvated ICs used for AIMS simulations, at the α(0.67)-SA3-CASSCF(4,3)/6-31G* level. Individual sticks for gas-phase (FWHM of 0.07 eV) and aqueous (FWHM of 0.40 eV) systems were convolved with a Gaussian envelope based on experimental FWHM. Simulated gas-phase data was taken from List *et al.*,[24] sampling from a 300 K harmonic Wigner distribution and using α(0.64)-SA3-CASSCF(4,3)/6-31G*. Experimental gas-phase and solvated chromophore spectra were obtained by digitizing data from Nielsen *et al.*[104] and Andersen *et al.*,[95] respectively. (b) Ground-state radial distribution functions of HBDI$^-$ heteroatoms (highlighted in each panel and identified in Fig. 1) in water. Shaded regions represent the first solvation shell. The dotted line represents a value of one, indicating that the solvent has reached bulk-like behavior.
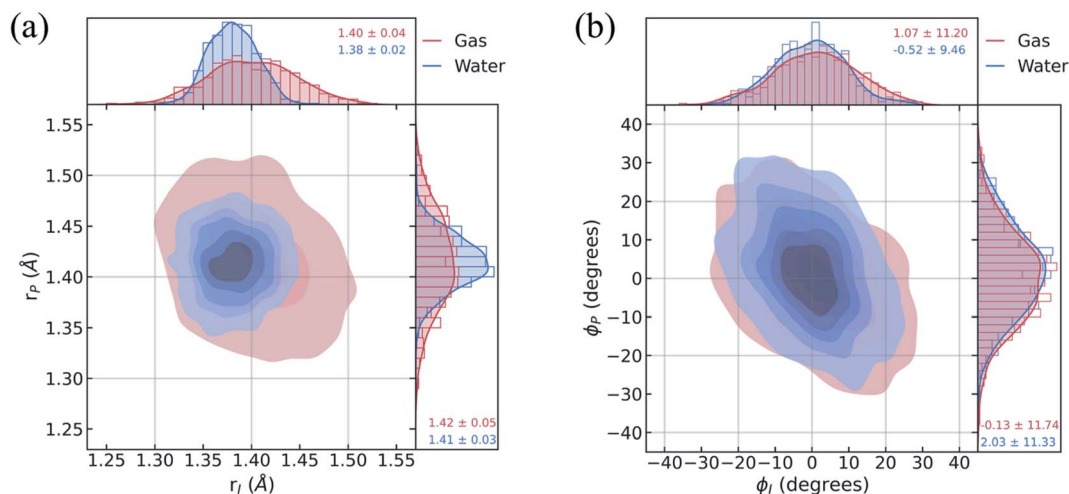
Fig. 4 Geometric characterization of ICs using the ground-state distributions of (a) carbon–carbon methine bridge bonds adjacent to the imidazolinone (r_I) and phenolate (r_P) rings and (b) dihedral angles associated with imidazolinone (ϕ_I) and phenolate (ϕ_P) twisting. Red indicates data for ICs sampled from a gas-phase harmonic Wigner distribution at 300 K. Blue indicates data for ICs sampled from aqueous QM/MM-MD simulations at 300 K (*via* a Boltzmann sampling procedure).

Although the difference in time scales of HBDI$^-$ intramolecular vibrations and solvent relaxation (*e.g.* time constants of 0.16 and 1.2 ps were reported for solvent relaxation following photoexcitation of a coumarin dye[106]) means that an equilibrium picture is unlikely to pertain to the dynamics induced by photoexcitation, an excited-state PMF identifies the energetically favored configurations of aqueous HBDI$^-$ following excitation. In other words, the PMF indicates the stability of twisted HBDI$^-$ structures that are surrounded by (partially or fully) relaxed solvent configurations. Such insight is useful for categorizing stable excited-state intermediates and interpreting the photodynamics of aqueous HBDI$^-$.

Fig. 5 Relative free energy profile on S_1 obtained from two-dimensional umbrella sampling along ϕ_I and ϕ_P. The zero point (marked with an "X") corresponds to the planar structure. The observed deactivation pathways through I-twisting (red) and P-twisting (green) are depicted schematically. For reference, arrows with dashed lines represent deactivation pathways observed in gas-phase simulations.[24]

The two-dimensional S_1 umbrella sampling along the bridge dihedrals in Fig. 5 shows that single-bond twisting about either of the bridge bonds is favored. The resulting PMF highlights four energetic wells located near 90° I- and P-twisted structures on S_1. Interestingly, the excited-state dynamics do not follow the minimum free energy path to reach these energetic wells (*vide infra*). Instead, the chromophore reaches highly-twisted configurations by following either the I- or P-channels illustrated in Fig. 5. Compared to the gas-phase photodynamics of HBDI$^-$,[24] the solvated chromophore exhibits more pronounced hula-twist-like (concerted single- and double-bond rotation) motion out of the FC region.

To separate out the electronic effects of equilibrium solvation, Fig. 6 displays the average S_0/S_1 energy gap across all windows in solvent and solvent-stripped configurations. In water (Fig. 6a), the observed minima along ϕ_I lie close to the CI seam, whereas rotation along ϕ_P leads to minima on S_1 that are ~1 eV removed from S_0. This suggests that the I-twisted CI seam is more peaked than the P-twisted CI seam. The absence of electronic degeneracy associated with P-twisting hints that energetically and/or entropically unfavorable geometric changes are required to reach degeneracy along this pathway. Fig. 6b shows that I-twisted intermediates have lower S_0/S_1 energy gaps than those of P-twisted intermediates in the gas-phase, as observed in solution. This energetic asymmetry originates from the differences in electron affinity between the I- and P-rings.[24] However, to conclude whether or not water stabilizes one twisted structure over the other, it is necessary to look at the energetic differences caused by solvation. The difference between water and gas-phase energy gaps (Fig. S9†) reveals that water introduces non-selective gap reduction (~0.3 eV) for highly-twisted (~90°) structures—the I- and P-twisted energy gaps decrease by approximately the same amount upon solvation. Yet, as previously discussed for Fig. 6a, the consequences of this gap reduction are significant. This
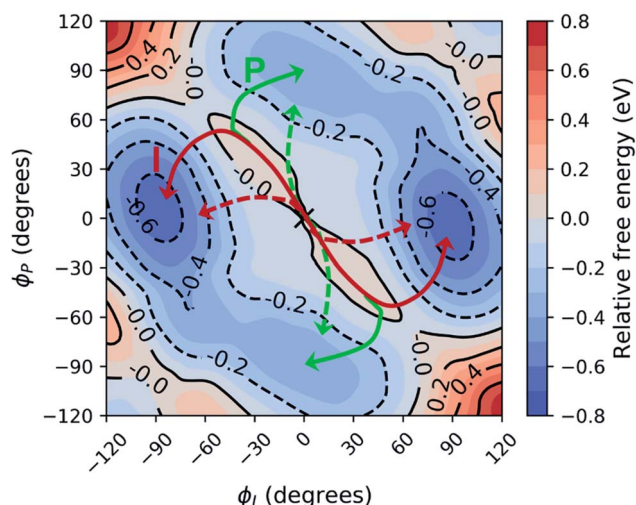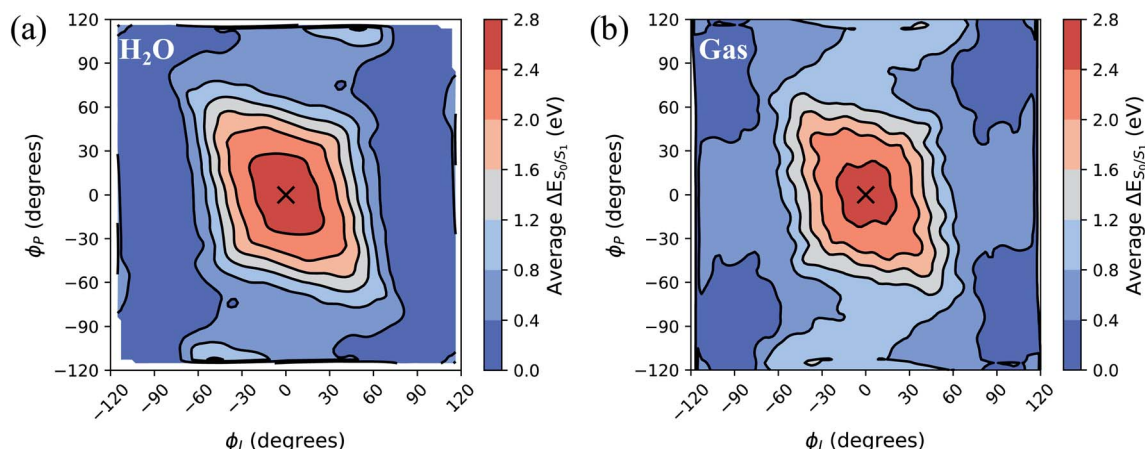
Fig. 6 Contour plot of the average S_0/S_1 energy gap with respect to ϕ_I and ϕ_P dihedral angles (a) in water and (b) in gas-phase. Gas-phase energies correspond to solvated structures (5000 points total, 8 per window) from (a) after removing the solvent around the chromophore. The average dihedral angles and energy gaps were plotted for each 10° window from the umbrella sampling, and cubic interpolation was performed between these points. The zero point (marked with an "X") corresponds to the planar structure. All energies were computed with $\alpha(0.67)$-SA3-CASSCF(4,3)/6-31G*.

equilibrium solvation picture suggests that (i) aqueous HBDI⁻ proceeds along one-bond-flip-dominated coordinates toward the twisted CI seam, as in gas-phase,[24] (ii) the I-twisted CI seam is more accessible than its P-twisted counterpart, and (iii) solvation promotes internal conversion through the I-twisted CI seam, similar to its neutral counterpart.[55,56] Our nonadiabatic dynamics simulations of HBDI⁻ show that (ii) and (iii) occur in water, while there is no evidence for (i). Rather than participating in a predominantly one-bond-flip mechanism (as in gas-phase), aqueous HBDI⁻ reaches CI seams *via* an aborted hula-twist-like motion out of the FC region. Note that the concerted torsion is conrotatory as opposed to the more usual (for the hula-twist mechanism) disrotatory motion.

Fig. 7 Ground- and excited-state populations during AIMS simulations. Fifty ICs were used for the explicitly-solvated system. The average state population is represented with solid lines. The vertical, gray dashed line represents the time at which population transfer begins. The black dotted line is the delayed bi-exponential fit to the S_1 population decay. Error bars are illustrated using transparent lines.

Nonadiabatic dynamics of HBDI⁻ in water

Shifting into the non-equilibrium regime (*i.e.*, the solvent may not have enough time to relax around the chromophore), we analyze the behavior of aqueous HBDI⁻ following photoexcitation. As shown by the S_1 population decay in Fig. 7, over half of the excited-state population is transferred to the ground state within the first 1 ps. Such a rapid decay is consistent with the ultrafast deactivation reported in experiments.[27,31,44] Yet, despite the sub-ps deactivation, a fraction of the population remains on the excited state for >5 ps. This biphasic pattern inspired a delayed bi-exponential fit to the decay profile:

$$P(t) = A \exp\left(-\frac{t - \tau_0}{\tau_1}\right) + (1 + A)\exp\left(-\frac{t - \tau_0}{\tau_2}\right) \quad (2)$$

where t represents time, A is a weighting coefficient, τ_0 represents the time at which population transfer begins (lagtime), and τ_1 and τ_2 are characteristic lifetimes associated with the decay of the S_1 population over time, $P(t)$. Constants obtained from this fitting procedure, through the use of bootstrapping, are: $A = 0.50 \pm 0.19$, $\tau_0 = 204 \pm 43$ fs, $\tau_1 = 609 \pm 181$ fs, and $\tau_2 = 3.1 \pm 1.2$ ps.

Viewing the dynamics within defined time intervals reveals novel information regarding the time scales of each deactivation pathway available to aqueous HBDI⁻—two distinct subpopulations exist with different excited-state lifetimes (Fig. 8). In accordance with the decreased electronic density along the methine bridge upon excitation (see Fig. 2) facile rotation along ϕ_I and ϕ_P is permitted on the excited state. Monitoring the S_1 population over time, with respect to the ϕ_I and ϕ_P dihedrals, illustrates (i) the accessibility and (ii) the population transfer efficiency of each internal conversion pathway. During the first 100 fs, the S_1 wavepacket remains localized near the FC region. Rather than following the minimum energy path along one-bond-flip coordinates (Fig. 5), the conrotatory hula-twist-like motion exhibited during the ground-state dynamics (Fig. 4b)
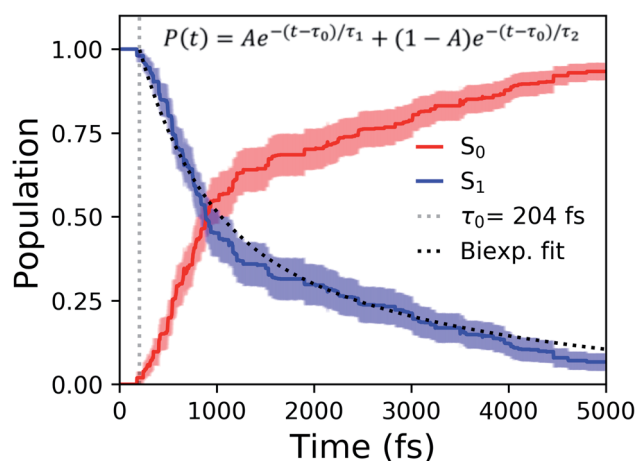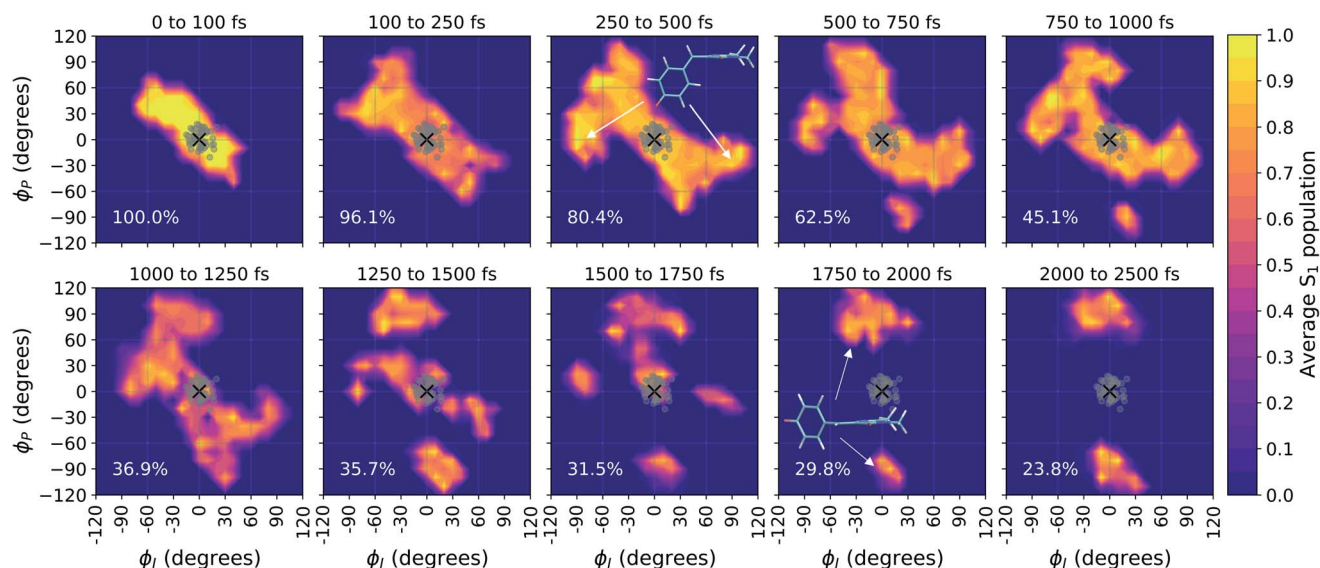
Fig. 8 Time evolution of the reduced S_1 density along the bridge dihedrals during the first 2.5 ps of solution–phase AIMS dynamics. Average dihedral angles and S_1 populations were computed using 10° intervals, and linear interpolation was performed between these points. The percentages displayed in each panel represent the total S_1 population at the end of the specified time window, relative to their maximum at time = 0 fs. Gray dots indicate the dihedral angles of the fifty initial conditions.

is preserved. This indicates a non-equilibrium solvation regime where the response of the surrounding waters is too slow to impede the concerted rotation of ϕ_I and ϕ_P out of the FC region, which is otherwise associated with a small free energy barrier (less than 0.2 eV). Once the free energy barrier along this path becomes too large to overcome, the wavepacket bifurcates *via* a process that involves a one-bond-flip-like rotation along either ϕ_I or ϕ_P – with one path leading to highly I-twisted structures (I-channel) and the other path leading to highly P-twisted structures (P-channel). The branching associated with this mechanism becomes apparent by 500 fs as exploration into the I- and P-channels enables population transfer to the ground state. By 1 ps, motion along the torsional angles is more prominent as the

I- and P-channels arise as the exclusive avenues for population transfer. Essentially no TBFs occupy near-planar configurations after 1.75 ps of dynamics, as four distinct regions in configuration space emerge as dihedral basins. These basins coincide with the energetic wells identified in Fig. 5. Interestingly, 250 fs later, no evidence of the I-twisted species is present while the P-twisted species remains on S_1 for several picoseconds. The disappearance of the I-twisted species on S_1 is explained by an ultrafast population transfer to the ground state, permitted by the near-degeneracy highlighted in Fig. 6a. For this part of the wavepacket, twisting along ϕ_I is enough to induce population transfer to the ground state. The persistence of the P-twisted species for several picoseconds on the excited state signifies
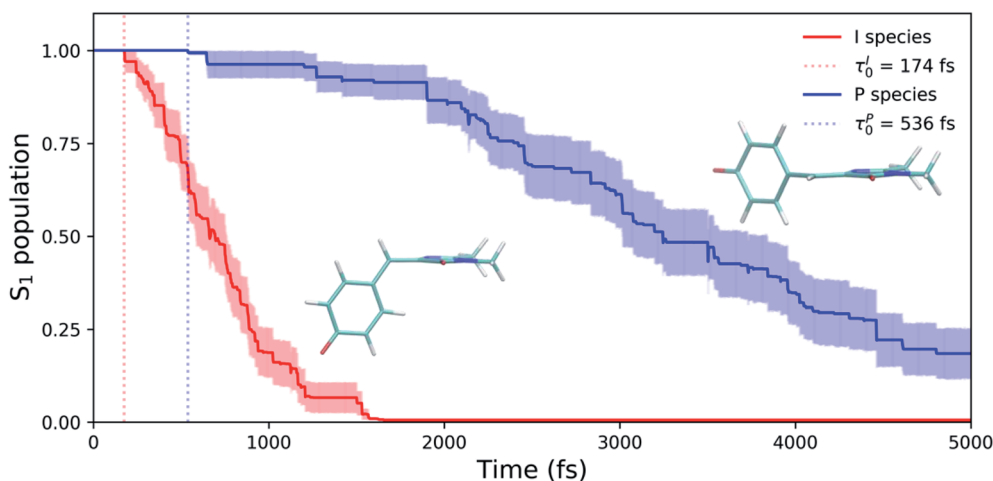

Fig. 9 Excited-state population decay of HBDI$^-$ in water for I- and P-deactivating ICs. Solid lines represent the average populations for each species. Transparent lines represent the error bars obtained from bootstrapping analysis. We indicate the delay time before population transfer (τ_0^I/τ_0^P) for each set with vertical dotted lines, emphasizing that deactivation is faster for I-twisting compared to P-twisting.

that dihedral torsion around ϕ_P alone is insufficient to facilitate efficient population transfer. Rather, additional geometric requirements are necessary for the P-species to participate in internal conversion.

The time scale differences established in Fig. 8 were refined using the S_1 population profiles for the I- and P-deactivating species (Fig. 9). In the case of I-twisted deactivation, the entire excited-state population is transferred to the ground state within ∼1.5 ps, with decay initiating at ∼175 fs. This rapid initiation and conclusion of population transfer for the I-species is due to an easily accessible I-twisted CI seam that efficiently transfers population to the ground state, in accordance with Fig. 6. On the other hand, the P-deactivation mechanism is associated with a species that remains on S_1 for ∼540 fs before population transfer begins. Furthermore, this mode of population transfer is much slower and less efficient, as ∼10% of the population remains on the excited state after 5 ps. A similar analysis compares the deactivation of red-shifted and blue-shifted ICs (Fig. S10, and Table S6†). Data from this partitioning approach suggests that blue-shifted ICs deactivate faster than red-shifted ICs, but further investigations are required to reach a definitive conclusion.

After identifying the characteristic twisting pathways, the dynamics out of the FC region were probed using various electronic and geometric parameters (Fig. 10, and S11†). Here, the parent TBFs are partitioned into I- and P-twisted species based on whether the I- or P-channel was taken, respectively. Our results corroborate that the dominant mode of deactivation (66%) is through torsion along ϕ_I, in agreement with nonadiabatic dynamics simulations at the XMS-CASPT2 (ref. 42) and spin-flip time-dependent density functional theory[43] levels. The violin plots in Fig. 10 present the distribution of key electronic and geometric observables sampled across all parent TBFs of each species during the first 500 fs. Characteristic activity along the ϕ_I and ϕ_P twisting dihedrals is observed within the first 500 fs. As expected, the I-species samples along ϕ_I more aggressively than it does along ϕ_P, and the opposite behavior is true for the P-species. Worth noting, however, is the time scale at which both species reach ∼90° rotations of their respective dihedrals. Between 200 and 400 fs, both species begin to explore and populate these highly twisted configurations. As in the gas-phase,[35] we observe that twisting along ϕ_I facilitates CT from the I-ring to the P-ring while twisting along ϕ_P facilitates CT from the P-ring to the I-ring. Furthermore, the molecule's rapid approach toward highly I- and P-twisted structures indicates that access to their respective TICT states is downhill in solution.
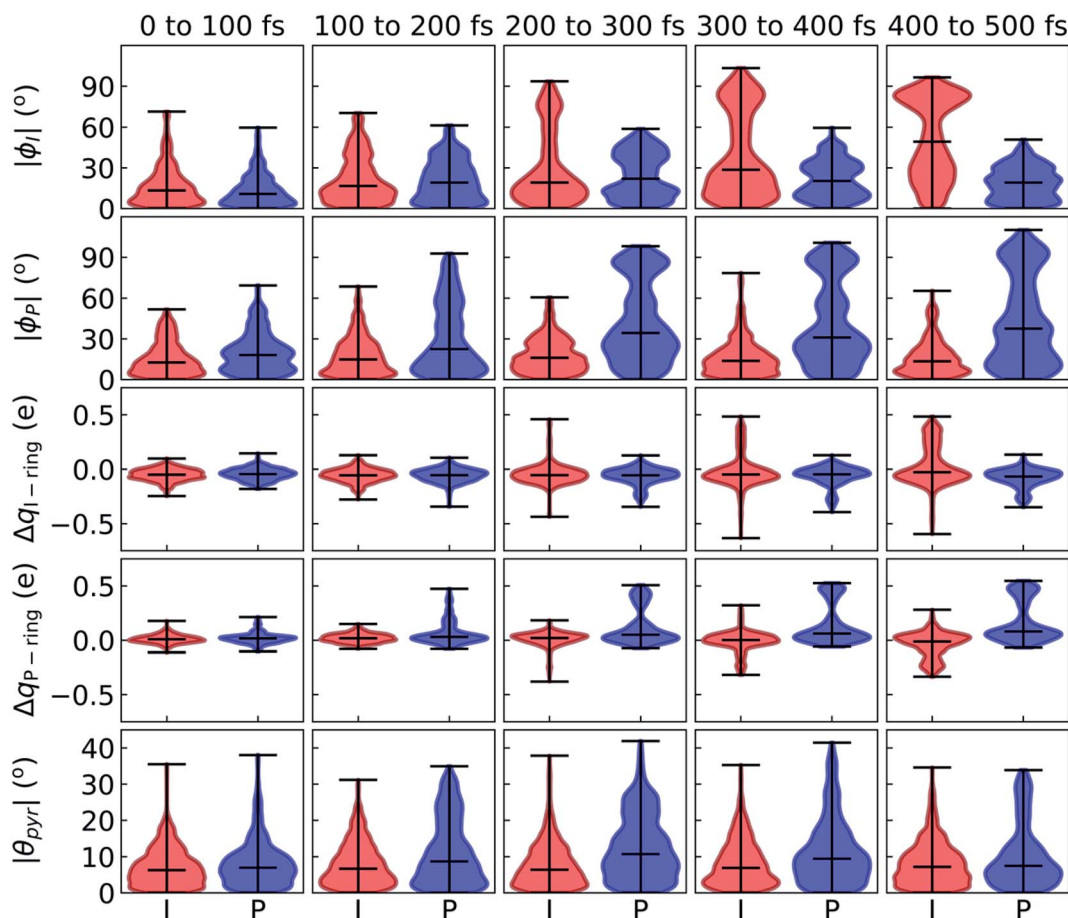

Fig. 10 Violin plots that monitor density distributions of geometric and electronic observables out of the FC region for I-deactivating (red) and P-deactivating (blue) species. Shown data monitors observables for the parent TBFs from each IC during the first 500 fs.

In the gas-phase, bond length alternation and bridge pyramidalization are the main coordinates used by HBDI$^-$ to reach the CI seam from the respective twisted S_1 minimum.[24] As shown in Fig. 10 (300–500 fs), displacement along the pyramidalization coordinate is attenuated for the I- and P-twisted species in solution relative to gas-phase ($|\theta_{pyr}|$ of 30° and 48° for I- and P-twisted MECIs,[24] respectively). Because solvation essentially closes the energy gap of the I-twisted species but not completely for the P-twisted, the bridge pyramidalization requirement for reaching the I-twisted CI seam essentially vanishes. Compared to species along the I-channel, larger-amplitude displacements of the pyramidalization coordinate are required to trigger population transfer along the P-channel. This suggests that the path to the I-twisted CI seam is essentially energetically downhill, while it is uphill for the P-twisted case.

In addition to monitoring the geometric and electronic changes that occur during the first few hundred femtoseconds following photoexcitation, the response of the solvent during the first 1 ps was investigated. Fig. 11 shows the evolution of the first solvation peak for the parts of the wavepacket following the I- and P-twisted pathways. In the case of the I-deactivating species in Fig. 11a, there are no significant changes to the RDF profiles of O_P, O_I, or N_I during the first 1 ps. This contrasts the evolution of RDFs for the same atoms in the P-deactivating species in Fig. 11b. Over the first 1 ps, the maximum of the first solvation peak for O_P and O_I gradually decreases and increases, respectively, toward the RDFs associated with equilibrated ϕ_P-twisted structures. This trend is consistent with the TICT behavior identified in Fig. 10. Upon torsion along ϕ_P, CT occurs from the P-ring to the I-ring. Consequently, a P-twisted intermediate will have (i) a more negative I-ring and (ii) a more positive P-ring than its pre-twisted counterpart. Thus, it is expected that the surrounding solvent would rearrange to compensate for this CT process by shifting increased solvent density from the O_P atom toward the O_I atom. Interestingly, the opposite trend is absent for the I-species. We attribute this

difference to the disparate deactivation time scales along ϕ_I and ϕ_P that are presented in Fig. 9. Because deactivation through the I-channel occurs so rapidly, water does not have time to relax fully around I-twisted structures before internal conversion. Furthermore, we suspect that the ground-state solvent arrangement (Fig. 3b) is beneficial for facilitating ultrafast deactivation *via* I-twisting, since water is already preferentially localized around the P-ring prior to TICT. Such behavior explains the absence of large shifts of excited-state RDF peaks in Fig. 11a. On the other hand, deactivation through the P-channel is more gradual than decay through the I-channel, due to the barrier between the P-twisted CI seam and the corresponding TICT intermediate. Consequently, the solvent has time to reorient itself around P-twisted structures on the excited state. As a result, we observe gradual shifts of excited-state RDF peaks in Fig. 11b.

A geometric analysis at the points of population transfer elucidates the difference between the deactivation profiles of the I- and P-species. For I-deactivation, the spawning events that lead to population transfer generally occur near geometries with ϕ_I angles near 90° and ϕ_P angles that lie relatively close to planarity, and *vice versa* for P-deactivation (Fig. 12). The relationship between key dihedral and pyramidalization angles reveals that, in addition to lasting longer on S_1, P-twisted TBFs demand larger pyramidalization angles than I-twisted TBFs to reach their respective CI seams. To investigate the implications of this difference, the absolute population transfer was calculated for each spawning event as a function of the pyramidalization and dihedral angle values upon entering the spawning region (Fig. 12a). Movie S1† provides a time lapse of these population and angle parameters to clarify this point. For a direct comparison of the spawned geometries associated with each pathway, the pyramidalization angle was measured for each spawned geometry of I-deactivating (Fig. 12b) and P-deactivating (Fig. 12c) TBFs. From these distributions, it is clear that pyramidalization requirements for P-deactivating
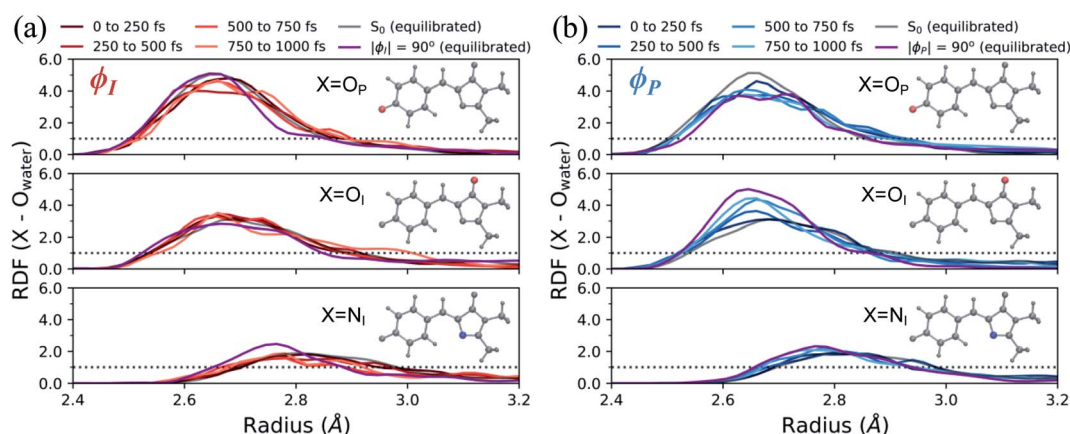

Fig. 11 Radial distribution functions of HBDI$^-$ heteroatoms in water during the first 1 ps of AIMS dynamics on S_1. Each RDF shown for (a) I-deactivating species and (b) P-deactivating species begins and ends within the specified time window. Each figure focuses on the first solvation shell of the specified atom. The equilibrated ϕ_I- and ϕ_P-twisted RDFs are obtained from umbrella sampling windows on S_1, with the specified angle restrained to ±90° while the other dihedral is restrained to zero degrees. The purple line represents the average of the 90°- and −90°-twisted RDFs on S_1. The dotted line represents a value of one, indicating that the solvent has reached bulk-like behavior.
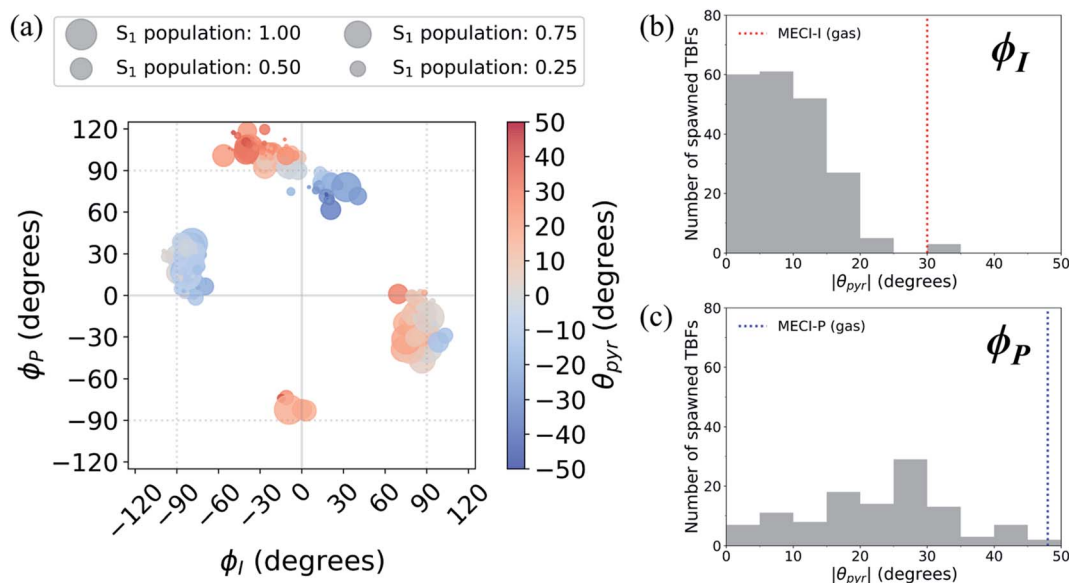
Fig. 12 (a) Absolute population transfer and pyramidalization angle associated with the bridge carbon atom for spawned geometries of aqueous HBDI$^-$ from parent TBFs. Absolute population transfer is defined by the fraction of original S_1 population transferred to S_0. Plotted values of ϕ_I, ϕ_P, and θ_{pyr} characterize geometries that initiate population transfer. A histogram (using 5° bins) of pyramidalization angle magnitudes is provided for spawned TBFs that transfer population through torsion dominated by (b) ϕ_I or (c) ϕ_P twisting. Pyramidalization angles measured for I- and P-twisted MECIs in gas–phase[24] are represented with vertical lines in (b) and (c).

TBFs are more demanding (peaked at ∼30°) than the requirements for I-deactivating TBFs (peaked at ∼10°). The larger pyramidalization angles needed to reach the P-twisted CI gate access to the P-twisted region of the CI seam. Therefore, we conclude that limited access to an uphill CI seam is responsible for the lingering S_1 population of the P-species.

In addition to being more accessible than the P-twisted CI seam, the I-twisted CI seam appears to be more efficient at transferring population to the ground state. On average, population transfer events mediated by the I- and P-channels transfer $56 \pm 32\%$ and $35 \pm 26\%$ of the incoming S_1 population to S_0 per spawning event, respectively (Fig. S12†). This is expected based on the more direct approach toward the I-twisted CI seam, than for its P-twisted counterpart, as supported by Fig. 5 and 6. The uphill pyramidalization requirements and lack of efficiency explain the more gradual deactivation of the P-twisted species.

Relative to gas-phase HBDI$^-$,[24] aqueous HBDI$^-$ generally demands less pyramidalization to reach I- and P-twisted CI seams (Fig. 12b and c). This difference between systems becomes most apparent when comparing internal conversion tendencies associated with the I-channel. In gas-phase, I-twisted configurations transfer population to S_0 while sampling along a larger range of ϕ_P values than in water. Based on our analysis regarding pyramidalization gating, we conclude that this behavior is due to the topology differences of the I-twisted CI seam across systems. Because solvation reduces the S_0/S_1 energy gap for I-twisted structures, aqueous HBDI$^-$ has smaller pyramidalization requirements to reach the I-twisted CI seam than does gas-phase HBDI$^-$. Thus, I-twisted structures of the solvated chromophore spend less time sampling ϕ_P torsion

than their gas-phase counterparts, as they undergo internal conversion through a near-barrierless process. The I-twisted spawning geometries of aqueous HBDI$^-$, which are associated with ultrafast population transfer, are consistent with rapid accessibility out of the FC region *via* an aborted hula-twist-like mechanism (as presented in Fig. 8). Because reaching the aqueous P-twisted CI seam from a P-twisted TICT intermediate is an energetically uphill process, P-twisted intermediates significantly sample configurations where ϕ_P is above 90°. The enhanced sampling along this coordinate may explain the higher proportion of spawning geometries skewed toward the *E*-isomer, relative to this proportion for ϕ_I from I-twisted spawns (Fig. S13†).

Based on vibrational signatures obtained from FSRS experiments, Taylor *et al.* proposed that the formation of a CS species and the transition from this CS state to a TICT state were responsible for measured short (∼350 fs) and long (∼2–3 ps) time components, respectively.[31] Our data suggests a different origin of these time constants. As supported by the substantial torsional displacements sampled within the first ∼200 fs (Fig. 10), the formation of TICT states is essentially barrierless. In other words, we do not see evidence of a non-twisted CS intermediate in water. Rather, we observe two competing processes: (i) an I-twisting process that easily reaches a downhill CI seam and (ii) a P-twisting process that encounters a barrier as it approaches an uphill CI seam. As an alternative, we propose that the accessibility of the I- and P-twisted CI seams, from the corresponding TICT states, is the primary factor responsible for the short (caused by mainly I-species) and long (caused by mainly P-species) time components reported from the FSRS experiments. However, rigorously establishing this
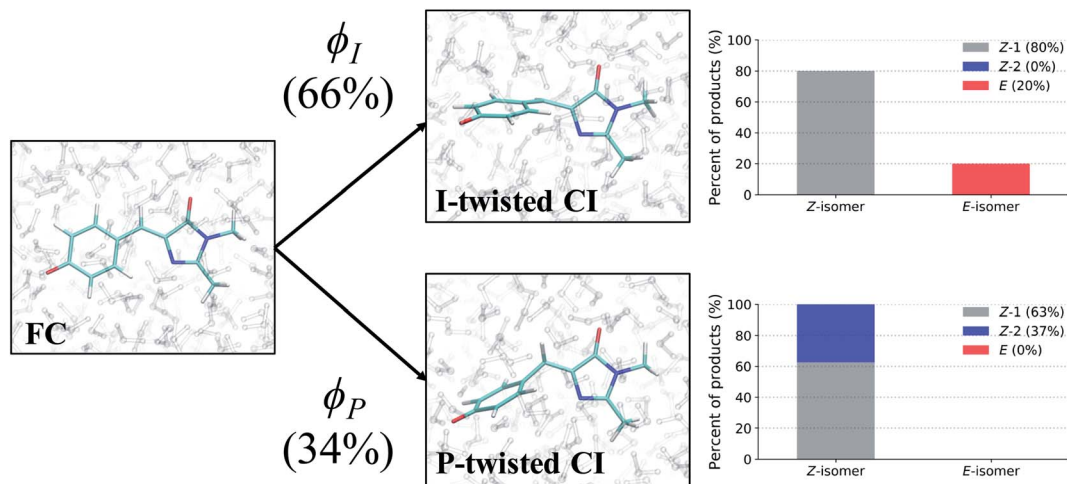
Fig. 13 Photoproducts of HBDI$^-$ in water for spawned TBFs, following 500 fs of QM/MM-MD on S$_0$. A total of 264 spawned TBFs were analyzed. ϕ_I and ϕ_P branching percentages represent the fraction of ICs that participated in each twisting pathway. Bar graphs illustrate the percentage of each product formed by the spawned TBFs for their respective pathway. The Z-1 product represents a Z-isomer of HBDI$^-$ that is not the result of Z/Z isomerization, whereas the Z-2 product corresponds to a Z-isomer of HBDI$^-$ following Z/Z isomerization.

interpretation of the FSRS fingerprints requires calculation of the vibrational signatures of I- and P-twisted structures and remains a task for future work.

Photoproducts

To evaluate the branching ratio of HBDI$^-$ upon deactivation to the ground state, dynamics on S$_0$ were continued for an
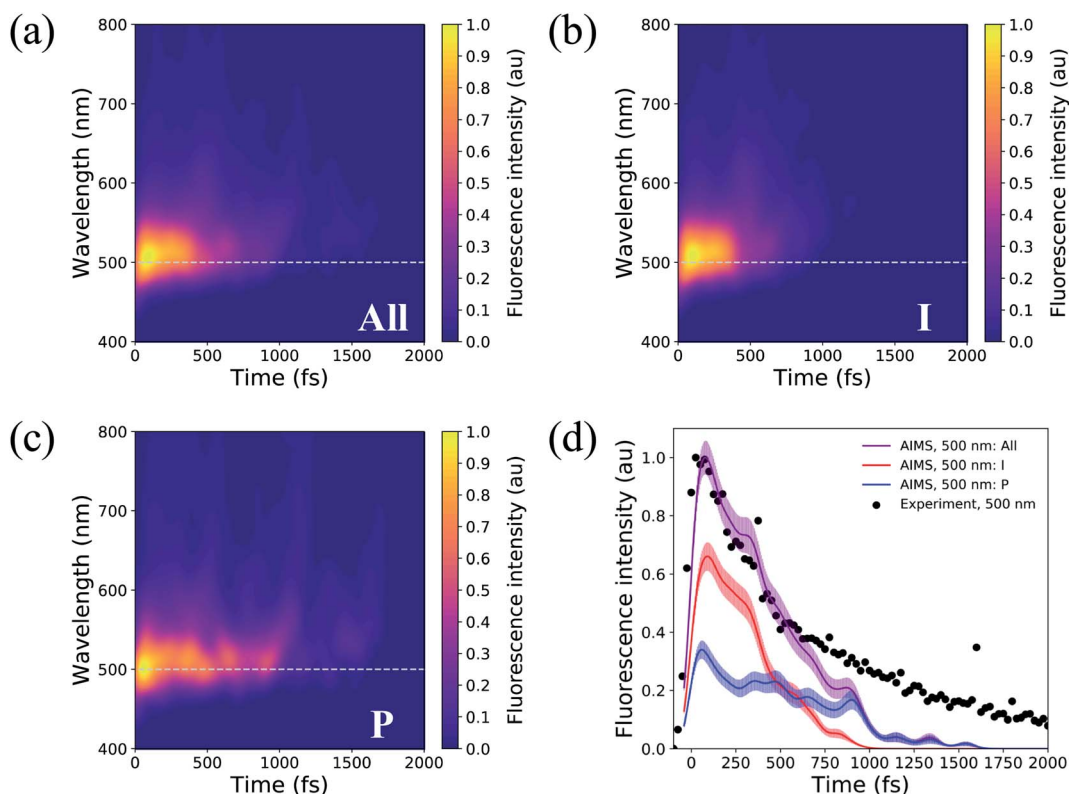

Fig. 14 Two-dimensional fluorescence spectrum, probed at 500 nm, for (a) all TBFs, (b) I-deactivating TBFs, and (c) P-deactivating TBFs. (d) Time-resolved fluorescence signals of HBDI$^-$ calculated from AIMS simulations in water. The maximum fluorescence intensities of I- and P-deactivating species are scaled based on the relative proportion of ICs that deactivate through the I- and P-channels. Experimental data, following 400 nm excitation, for HBDI$^-$ in water was provided by Meech and co-workers.[27,103] To align the experimental[31] and theoretical fluorescence wavelength maxima, a shift of 0.13 eV was applied to the theory spectra (Fig. S15†). Transparent lines represent the error obtained from bootstrapping analysis.

additional 500 fs (Fig. S14, and Table S7†). Classifying the resulting products provides an estimate for the branching ratio with respect to Z/E isomerization, Z/Z isomerization, and ground-state recovery of the Z-isomer. Most of the population (87%) returns to the Z-isomer (Fig. 13), in line with the low Z/E isomerization quantum yield reported from experiments.[44–46] Despite I-torsion being the dominant deactivation pathway, associated CIs are highly inefficient at producing E photo-products. Thus, HBDI$^-$ is much less efficient at generating E photoproducts in solution (~13% yield) than in gas-phase (~30% yield).[24] Only 20% of the I-twisted spawns undergo Z/E isomerization. P-twisted CIs are more efficient (37%) at producing P-flipped products; however, the symmetry of the P-ring regenerates the Z-isomer whether or not the P-ring isom-erizes. Verifying the Z/Z isomerization quantum yield experi-mentally would require asymmetric substitution on the P-ring. The respective isomerization quantum yields are likely linked to the barrier (or lack thereof) between the TICT state and CI seam associated with each pathway. Because the I-twisted CI seam is reached without significant pyramidalization, I-twisted struc-tures readily proceed through the CI seam as soon as twisting along ϕ_I nears 90° (Fig. S13a†). On the other hand, the P-twisted CI seam is not reached so easily. As a consequence, P-twisted intermediates sample along ϕ_P more robustly to reach signifi-cantly pyramidalized structures. This results in a majority of spawns with ϕ_P greater than 90° (Fig. S13b†) and likely

contributes to the higher quantum yield for Z/Z isomerization than that of E/Z isomerization.

Time-resolved fluorescence

Solvated HBDI$^-$ has been the subject of many time-resolved fluorescence experiments.[27,37,107–109] To link our simulation data to experimental findings, time-resolved fluorescence spectra were computed over the course of the AIMS simulations (Fig. 14). A line out at 500 nm (based on experiment[103]) is extracted for various sets of TBFs. Across all TBFs (Fig. 14a), the two-dimensional fluorescence spectrum experiences a signifi-cant red-shift spectral evolution after a few hundred femtosec-onds. The red-shift and the reduction in fluorescence signal are attributed to a decrease in the S_0/S_1 energy gap and emission strength, respectively, as the chromophore begins twisting its bridge dihedrals upon departure from the FC region (Table S3, and Fig. S16†). Since twisting along ϕ_I and ϕ_P is correlated with a decrease in oscillator strength, we expect that the steeper (compared to XMS-CASPT2) α-CASSCF gradients beyond 30° torsion of ϕ_I and/or ϕ_P (Fig. S1†) artificially accelerate fluores-cence quenching in our AIMS simulations. The fluorescence spectrum was decomposed to obtain the contributions from the I- and P-deactivating species (Fig. 14b, and c). By comparing the two-dimensional fluorescence spectra, it becomes obvious that the P-twisted channel significantly prolongs the fluorescence intensity of aqueous HBDI$^-$ when compared to the signal from
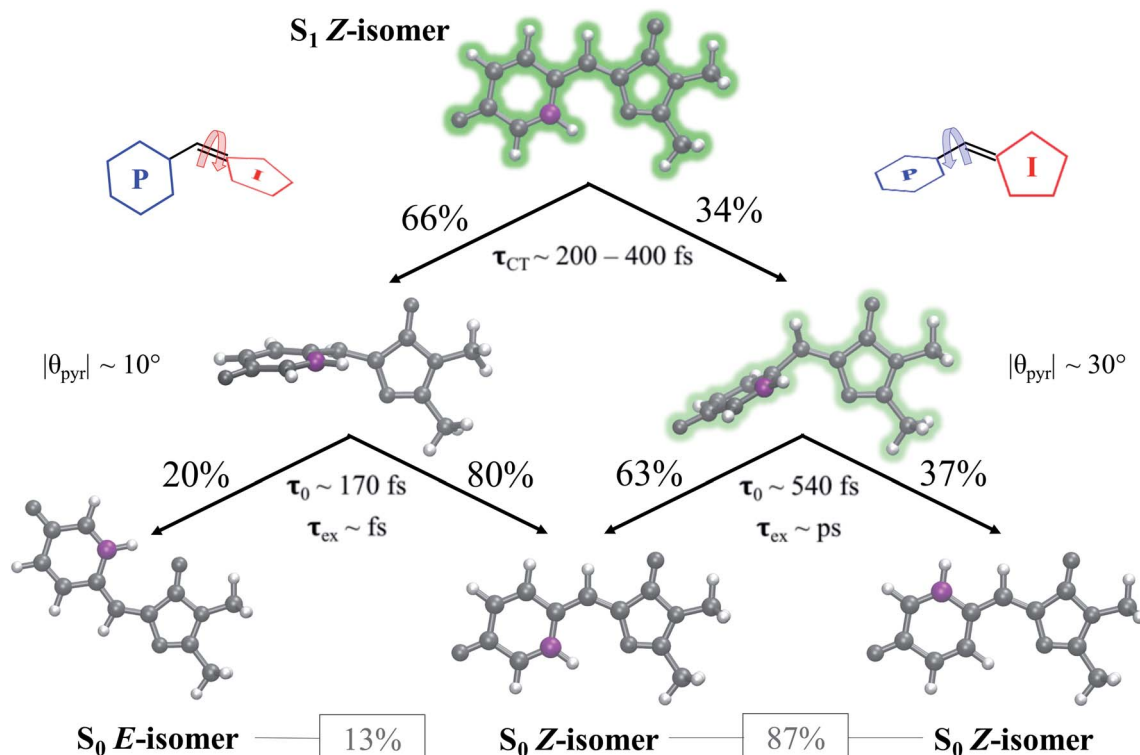

Fig. 15 Summary of the photophysics of the solvated GFP chromophore. Percentages indicate the relative population that proceeds along a given pathway. τ_{CT} represents the time range at which TICT occurs, τ_0 represents the time at which population transfer begins, and τ_{ex} represents the order of the excited-state lifetime. θ_{pyr} represents the peak in the pyramidalization angle distribution for spawned geometries. Heavy atoms are colored gray, hydrogen atoms are colored white, and a reference carbon atom is colored purple to distinguish P-ring-flipped and original Z products. Percentages listed in boxes indicate the total percent of spawned TBFs that formed the associated photoproduct.

the I-twisted channel. From the time-resolved fluorescence spectrum for all TBFs at 500 nm (Fig. 14d), AIMS simulations predict a fluorescence signal that loses roughly 50% of its intensity by 500 fs. Despite this rapid quenching, fluorescence signatures are observed beyond 1.5 ps. An I- and P-pathway decomposition of this signal shows that I-twisting species quench their fluorescence rapidly (within a picosecond). Yet, the P-twisting species has a more pronounced fluorescence signal that survives until ~1.6 ps. Therefore, the long-lived signal in the time-resolved spectrum, across all TBFs, is attributed to the species that undergoes internal conversion through the P-channel. We attribute the faster fluorescence decay of our simulations, relative to experiment, to the slightly steeper α-CASSCF gradients for partially twisted geometries, when compared to XMS-CASPT2. Furthermore, the underestimated S_0/S_1 energy gap for I- and P-twisted structures at the α-CASSCF level (Fig. S1†) likely red-shifts the fluorescence signal of I- and P-twisted structures more than expected. However, this issue likely affects the fluorescence signal of P-twisted TBFs, which remain on S_1 for several picoseconds, more than the signal of I-twisted TBFs. Another possible contributor to the faster-than-expected simulated fluorescence signal is a higher ratio of P-to-I species in experiment than sampled for our AIMS simulations, which would increase the intensity of the fluorescence tail. Despite these discrepancies, our simulations provide evidence that the deactivation pathway taken by the chromophore has a significant impact on the observed time-resolved fluorescence.

Conclusions

AIMS dynamics support the presence of two ground-state recovery mechanisms after the photoexcitation of aqueous HBDI$^-$ to S_1. The dominant mode of deactivation, through I-twisting, proceeds *via* an ultrafast mechanism and is responsible for the rapidly-decaying signals in time-resolved fluorescence and FSRS experiments. The minor pathway, through P-twisting, remains on S_1 for several picoseconds and its access to the CI seam is gated by pyramidalization of the central methine bridge carbon. Our results provide evidence for the following mechanism: (1) evolution from the FC region *via* near-barrierless motions that are consistent with ground-state QM/MM-MD simulations, (2) formation of a TICT state through an aborted hula-twist-like (conrotatory) mechanism as either ϕ_I or ϕ_P approaches 90°, (3) population transfer from S_1 to S_0 as the two states reach electronic degeneracy (through I-twisting for the I-species and through P-twisting along with pyramidalization for the P-species), and (4) re-population of the ground state with low Z/E and Z/Z isomerization quantum yields. This process is summarized in Fig. 15. The ultrafast differentiation between I- and P-species indicates that both twisted species are accessible from the FC region with little/no energetic barrier, as supported by Fig. 5 and S1.† Relative to the uphill approach needed to reach the P-twisted CI seam, the downhill approach to the I-twisted CI seam makes it easier to transfer population to the ground state through the I-channel. However, the P-twisted

species has an isomerization quantum yield about two times as large as its I-twisted counterpart.

Our AIMS simulations provide novel mechanistic and electronic insight into the behavior that governs the photodynamics of the GFP chromophore. QM/MM-MD simulations indicate that surrounding HBDI$^-$ with mobile solvent molecules has minimal impact on the configuration space sampled by the chromophore in water. Yet, the electronic effects of water blue-shift the absorption spectrum. During gas- and solution-phase dynamics on S_0, preferential twisting along ϕ_I and ϕ_P in a hula-twist-like (conrotatory) fashion is observed. The subsequent internal conversion mechanisms predominantly occur through rotation of ϕ_I in both systems.[24] The absence of rigid electronic and steric constraints on the chromophore likely explains the ultrafast deactivation tendencies reported by experiments for both systems.[21,27,30,31] However, the stabilization of highly-twisted structures and the promotion of electronic degeneracy, especially with respect to ϕ_I which results in a downhill CI seam, are responsible for shorter lifetimes in water when compared to gas-phase. Furthermore, the fitted time constants for the S_1 population decay (609 ± 181 fs and 3.1 ± 1.2 ps) are associated with internal conversion through the I- and P-channels, respectively. Through a direct comparison of AIMS simulations and experimental fluorescence spectra, we provide mechanistic insight to explain the observed fluorescence profile of HBDI$^-$ in water.[27] We attribute the short experimental time constant (210 fs) describing HBDI$^-$ fluorescence in water to the departure from the FC region (of both I- and P-deactivating species), while the longer experimental fluorescence time constant (1.1 ps) corresponds to the longer-lived, P-deactivating species.

Although our simulations do not include an explicit protein environment, our findings imply that the mobility and electronic distribution of residues surrounding the chromophore in a protein can tune the chromophore's behavior on the excited state. From our simulations, we predict that modifications to the protein environment can lead to internal conversion pathways with notably different population transfer rates, fluorescence profiles, and isomerization quantum yields. Using Dronpa2 variants, Romei and co-workers[110] have demonstrated that chromophore modifications can bias the preferred directionality of the CT process and modify observables of interest in the protein. Our direct observation of TICT processes in solution provides evidence that steering the chromophore toward a given pathway can significantly alter its properties. To characterize the photochemical processes that drive the dynamics of the chromophore in protein scaffolds, we will extend our simulations and analyses to fluorescent protein systems.

Author contributions

CMJ contributed to data curation, formal analysis, investigation, methodology, visualization and writing (original draft) of the presented work. NHL contributed to data curation, investigation, methodology and project administration. TJM contributed to methodology, project administration, funding

acquisition, resources, and supervision. All authors contributed to conceptualization of the project and review and editing of the manuscript.

Conflicts of interest

There are no conflicts to declare.

Acknowledgements

References

1 O. Shimomura, F. H. Johnson and Y. Saiga, *J. Cell. Comp. Physiol.*, 1962, **59**, 223–239.

2 F. H. Johnson, O. Shimomura, Y. Saiga, L. C. Gershman, G. T. Reynolds and J. R. Waters, *J. Cell. Comp. Physiol.*, 1962, **60**, 85–103.

3 J. G. Morin and J. W. Hastings, *J. Cell. Physiol.*, 1971, **77**, 313–318.

4 H. Morise, O. Shimomura, F. H. Johnson and J. Winant, *Biochemistry*, 1974, **13**, 2656–2662.

5 O. Shimomura, *FEBS Lett.*, 1979, **104**, 220–222.

6 M. Chalfie, Y. Tu, G. Euskirchen, W. W. Ward and D. C. Prasher, *Science*, 1994, **263**, 802–805.

7 S. Inouye and F. I. Tsuji, *FEBS Lett.*, 1994, **341**, 277–280.

8 R. Y. Tsien, *Annu. Rev. Biochem.*, 1998, **67**, 509–544.

9 B. J. Feilmeier, G. Iseminger, D. Schroeder, H. Webber and G. J. Phillips, *J. Bacteriol.*, 2000, **182**, 4068–4076.

10 J. Lippincott-Schwartz, E. Snapp and A. Kenworthy, *Nat. Rev. Mol. Cell Biol.*, 2001, **2**, 444–456.

11 J. Lippincott-Schwartz and G. H. Patterson, *Science*, 2003, **300**, 87–91.

12 W. W. Ward, H. J. Prentice, A. F. Roth, C. W. Cody and S. C. Reeves, *Photochem. Photobiol.*, 1982, **35**, 803–808.

13 R. Heim, D. C. Prasher and R. Y. Tsien, *Proc. Natl. Acad. Sci. U. S. A.*, 1994, **91**, 12501–12504.

14 R. Heim, A. B. Cubitt and R. Y. Tsien, *Nature*, 1995, **373**, 663–664.

15 R. Heim and R. Y. Tsien, *Curr. Biol.*, 1996, **6**, 178–182.

16 R. M. Dickson, A. B. Cubitt, R. Y. Tsien and W. E. Moerner, *Nature*, 1997, **388**, 355–358.

17 G. H. Patterson and J. Lippincott-Schwartz, *Science*, 2002, **297**, 1873–1877.

18 M. Hofmann, C. Eggeling, S. Jakobs and S. W. Hell, *Proc. Natl. Acad. Sci. U. S. A.*, 2005, **102**, 17565–17569.

19 S. Kojima, H. Ohkawa, T. Hirano, S. Maki, H. Niwa, M. Ohashi, S. Inouye and F. I. Tsuji, *Tetrahedron Lett.*, 1998, **39**, 5239–5242.

20 M. Chattoraj, B. A. King, G. U. Bublitz and S. G. Boxer, *Proc. Natl. Acad. Sci. U. S. A.*, 1996, **93**, 8362–8367.

21 A. Svendsen, H. V. Kiefer, H. B. Pedersen, A. V. Bochenkova and L. H. Andersen, *J. Am. Chem. Soc.*, 2017, **139**, 8766–8771.

22 F. Yang, L. G. Moss and G. N. Phillips Jr, *Nat. Biotechnol.*, 1996, **14**, 1246–1251.

23 M. Ormö, A. B. Cubitt, K. Kallio, L. A. Gross, R. Y. Tsien and S. J. Remington, *Science*, 1996, **273**, 1392–1395.

24 N. H. List, C. M. Jones and T. J. Martínez, 2021, DOI: 10.26434/chemrxiv.14544555.

25 M. A. Perozzo, K. B. Ward, R. B. Thompson and W. W. Ward, *J. Biol. Chem.*, 1988, **263**, 7713–7716.

26 G. Striker, V. Subramaniam, C. A. M. Seidel and A. Volkmer, *J. Phys. Chem. B*, 1999, **103**, 8612–8617.

27 D. Mandal, T. Tahara and S. R. Meech, *J. Phys. Chem. B*, 2004, **108**, 1102–1108.

28 A. Usman, O. F. Mohammed, E. T. Nibbering, J. Dong, K. M. Solntsev and L. M. Tolbert, *J. Am. Chem. Soc.*, 2005, **127**, 11214–11215.

29 C. W. West, A. S. Hudson, S. L. Cobb and J. R. Verlet, *J. Chem. Phys.*, 2013, **139**, 071104.

30 C. R. S. Mooney, D. A. Horke, A. S. Chatterley, A. Simperler, H. H. Fielding and J. R. R. Verlet, *Chem. Sci.*, 2013, **4**, 921–927.

31 M. A. Taylor, L. Zhu, N. D. Rozanov, K. T. Stout, C. Chen and C. Fang, *Phys. Chem. Chem. Phys.*, 2019, **21**, 9728–9739.

32 M. W. Forbes and R. A. Jockusch, *J. Am. Chem. Soc.*, 2009, **131**, 17038–17039.

33 H. Niwa, S. Inouye, T. Hirano, T. Matsuno, S. Kojima, M. Kubota, M. Ohashi and F. I. Tsuji, *Proc. Natl. Acad. Sci. U. S. A.*, 1996, **93**, 13617–13622.

34 M. E. Martin, F. Negri and M. Olivucci, *J. Am. Chem. Soc.*, 2004, **126**, 5452–5464.

35 S. Olsen, K. Lamothe and T. J. Martínez, *J. Am. Chem. Soc.*, 2010, **132**, 1192–1193.

36 N. M. Webber, K. L. Litvinenko and S. R. Meech, *J. Phys. Chem. B*, 2001, **105**, 8036–8039.

37 K. L. Litvinenko, N. M. Webber and S. R. Meech, *Bull. Chem. Soc. Jpn.*, 2002, **75**, 1065–1070.

38 W. Weber, V. Helms, J. A. McCammon and P. W. Langhoff, *Proc. Natl. Acad. Sci. U. S. A.*, 1999, **96**, 6177–6182.

39 R. S. Liu and A. E. Asato, *Proc. Natl. Acad. Sci. U. S. A.*, 1985, **82**, 259–263.

40 R. S. H. Liu and G. S. Hammond, *Chem.–Eur. J.*, 2001, **7**, 4536–4545.

41 P. Altoe, F. Bernardi, M. Garavelli, G. Orlandi and F. Negri, *J. Am. Chem. Soc.*, 2005, **127**, 3952–3963.

42 J. W. Park and T. Shiozaki, *J. Chem. Theory Comput.*, 2017, **13**, 3676–3683.

43 N. Minezawa and T. Nakajima, *J. Chem. Phys.*, 2020, **152**, 024119.
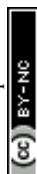
44 M. Vengris, I. H. M. van Stokkum, X. He, A. F. Bell, P. J. Tonge, R. van Grondelle and D. S. Larsen, *J. Phys. Chem. A*, 2004, **108**, 4587–4598.

45 J. S. Yang, G. J. Huang, Y. H. Liu and S. M. Peng, *Chem. Commun.*, 2008, 1344–1346, DOI: 10.1039/b717714c.

46 V. Voliani, R. Bizzarri, R. Nifosi, S. Abbruzzetti, E. Grandi, C. Viappiani and F. Beltram, *J. Phys. Chem. B*, 2008, **112**, 10714–10722.

47 B. G. Levine, C. Ko, J. Quenneville and T. J. Martínez, *Mol. Phys.*, 2006, **104**, 1039–1051.

48 E. F. Kjonstad, R. H. Myhre, T. J. Martínez and H. Koch, *J. Chem. Phys.*, 2017, **147**, 164105.

49 D. Tuna, D. Lefrancois, L. Wolanski, S. Gozem, I. Schapiro, T. Andruniow, A. Dreuw and M. Olivucci, *J. Chem. Theory Comput.*, 2015, **11**, 5758–5781.

50 J. W. Snyder Jr, R. M. Parrish and T. J. Martínez, *J. Phys. Chem. Lett.*, 2017, **8**, 2432–2437.

51 G. J. Atchity, S. S. Xantheas and K. Ruedenberg, *J. Chem. Phys.*, 1991, **95**, 1862–1876.

52 M. Ben-Nun, F. Molnar, K. Schulten and T. J. Martínez, *Proc. Natl. Acad. Sci. U. S. A.*, 2002, **99**, 1769–1773.

53 J. P. Malhado and J. T. Hynes, *J. Chem. Phys.*, 2016, **145**, 194104.

54 A. M. Virshup, J. Chen and T. J. Martínez, *J. Chem. Phys.*, 2012, **137**, 22A519.

55 A. Toniolo, G. Granucci and T. J. Martínez, *J. Phys. Chem. A*, 2003, **107**, 3822–3830.

56 A. Toniolo, S. Olsen, L. Manohar and T. J. Martínez, *Faraday Discuss.*, 2004, **127**, 149–163.

57 T. J. Martínez, M. Ben-Nun and R. D. Levine, *J. Phys. Chem.*, 1996, **100**, 7884–7895.

58 M. Ben-Nun and T. J. Martínez, *J. Chem. Phys.*, 1998, **108**, 7244–7257.

59 M. Ben-Nun, J. Quenneville and T. J. Martínez, *J. Phys. Chem. A*, 2000, **104**, 5161–5175.

60 M. Ben-Nun and T. J. Martínez, *Adv. Chem. Phys.*, 2002, **121**, 439–512.

61 B. F. E. Curchod and T. J. Martínez, *Chem. Rev.*, 2018, **118**, 3305–3336.

62 K. K. Docken and J. Hinze, *J. Chem. Phys.*, 1972, **57**, 4928–4936.

63 B. O. Roos, *Adv. Chem. Phys.*, 1987, **69**, 399–445.

64 J. W. Snyder Jr, E. G. Hohenstein, N. Luehr and T. J. Martínez, *J. Chem. Phys.*, 2015, **143**, 154107.

65 J. W. Snyder Jr, B. S. Fales, E. G. Hohenstein, B. G. Levine and T. J. Martínez, *J. Chem. Phys.*, 2017, **146**, 174113.

66 T. J. A. Wolf, D. M. Sanchez, J. Yang, R. M. Parrish, J. P. F. Nunes, M. Centurion, R. Coffee, J. P. Cryan, M. Guhr, K. Hegazy, A. Kirrander, R. K. Li, J. Ruddock, X. Shen, T. Vecchione, S. P. Weathersby, P. M. Weber, K. Wilkin, H. Yong, Q. Zheng, X. J. Wang, M. P. Minitti and T. J. Martínez, *Nat. Chem.*, 2019, **11**, 504–509.

67 L. M. Frutos, T. Andruniow, F. Santoro, N. Ferre and M. Olivucci, *Proc. Natl. Acad. Sci. U. S. A.*, 2007, **104**, 7764–7769.

68 S. Olsen and R. H. McKenzie, *J. Chem. Phys.*, 2009, **130**, 184302.

69 I. V. Polyakov, B. L. Grigorenko, E. M. Epifanovsky, A. I. Krylov and A. V. Nemukhin, *J. Chem. Theory Comput.*, 2010, **6**, 2377–2387.

70 W. J. Hehre, R. Ditchfield and J. A. Pople, *J. Chem. Phys.*, 1972, **56**, 2257–2261.

71 T. P. Radhakrishnan and I. Agranat, *Struct. Chem.*, 1991, **2**, 107–115.

72 J. Finley, P. A. Malmqvist, B. O. Roos and L. Serrano-Andres, *Chem. Phys. Lett.*, 1998, **288**, 299–306.

73 A. A. Granovsky, *J. Chem. Phys.*, 2011, **134**, 214113.

74 C. Song and T. J. Martínez, *J. Chem. Phys.*, 2020, **152**, 234113.

75 N. Gidopoulos and A. Theophilou, *Philos. Mag. B*, 1994, **69**, 1067–1074.

76 G. Granucci and A. Toniolo, *Chem. Phys. Lett.*, 2000, **325**, 79–85.

77 N. I. Gidopoulos, P. G. Papaconstantinou and E. K. U. Gross, *Physica B*, 2002, **318**, 328–332.

78 P. Slavicek and T. J. Martínez, *J. Chem. Phys.*, 2010, **132**, 234102.

79 J. Kastner, J. M. Carr, T. W. Keal, W. Thiel, A. Wander and P. Sherwood, *J. Phys. Chem. A*, 2009, **113**, 11856–11865.

80 I. S. Ufimtsev and T. J. Martínez, *J. Chem. Theory Comput.*, 2008, **4**, 222–231.

81 I. S. Ufimtsev and T. J. Martínez, *J. Chem. Theory Comput.*, 2009, **5**, 1004–1015.

82 I. S. Ufimtsev and T. J. Martínez, *J. Chem. Theory Comput.*, 2009, **5**, 2619–2628.

83 S. Seritan, C. Bannwarth, B. S. Fales, E. G. Hohenstein, S. I. L. Kokkila-Schumacher, N. Luehr, J. W. Snyder, Jr., C. Song, A. V. Titov, I. S. Ufimtsev and T. J. Martínez, *J. Chem. Phys.*, 2020, **152**, 224110.

84 S. Seritan, C. Bannwarth, B. S. Fales, E. G. Hohenstein, C. M. Isborn, S. I. L. Kokkila-Schumacher, X. Li, F. Liu, N. Luehr, J. W. Snyder, C. Song, A. V. Titov, I. S. Ufimtsev, L. P. Wang and T. J. Martínez, *Wiley Interdiscip. Rev. Comput. Mol. Sci.*, 2020, **11**, 1–16.

85 L. Martínez, R. Andrade, E. G. Birgin and J. M. Martínez, *J. Comput. Chem.*, 2009, **30**, 2157–2164.

86 P. Eastman, J. Swails, J. D. Chodera, R. T. McGibbon, Y. Zhao, K. A. Beauchamp, L. P. Wang, A. C. Simmonett, M. P. Harrigan, C. D. Stern, R. P. Wiewiora, B. R. Brooks and V. S. Pande, *PLoS Comput. Biol.*, 2017, **13**, e1005659.

87 Y. Wu, H. L. Tepper and G. A. Voth, *J. Chem. Phys.*, 2006, **124**, 024503.

88 I. S. Joung and T. E. Cheatham III, *J. Phys. Chem. B*, 2008, **112**, 9020–9041.

89 C. I. Bayly, P. Cieplak, W. D. Cornell and P. A. Kollman, *J. Phys. Chem.*, 1993, **97**, 10269–10280.

90 C. Lee, W. Yang and R. G. Parr, *Phys. Rev. B: Condens. Matter Mater. Phys.*, 1988, **37**, 785–789.

91 A. D. Becke, *J. Chem. Phys.*, 1993, **98**, 5648–5652.

92 S. Grimme, J. Antony, S. Ehrlich and H. Krieg, *J. Chem. Phys.*, 2010, **132**, 154104.

93 J. Wang, R. M. Wolf, J. W. Caldwell, P. A. Kollman and D. A. Case, *J. Comput. Chem.*, 2004, **25**, 1157–1174.

94 A. M. Niklasson, P. Steneteg, A. Odell, N. Bock, M. Challacombe, C. J. Tymczak, E. Holmstrom, G. Zheng and V. Weber, *J. Chem. Phys.*, 2009, **130**, 214109.

95 L. H. Andersen, A. Lapierre, S. B. Nielsen, I. B. Nielsen, S. U. Pedersen, U. V. Pedersen and S. Tomita, *Eur. Phys. J. D*, 2002, **20**, 597–600.

96 J. R. R. Verlet, Personal communication, 2019.

97 B. Efron and R. J. Tibshirani, *An Introduction to the Bootstrap*, Chapman and Hall/CRC, New York, 1st edn, 1994.

98 R. T. McGibbon, K. A. Beauchamp, M. P. Harrigan, C. Klein, J. M. Swails, C. X. Hernandez, C. R. Schwantes, L. P. Wang, T. J. Lane and V. S. Pande, *Biophys. J.*, 2015, **109**, 1528–1532.

99 B. Roux, *Comput. Phys. Commun.*, 1995, **91**, 275–282.

100 S. Kumar, J. M. Rosenberg, D. Bouzida, R. H. Swendsen and P. A. Kollman, *J. Comput. Chem.*, 1992, **13**, 1011–1021.

101 A. Grossfield, WHAM: an implementation of the weighted histogram analysis method, http://membrane.urmc.rochester.edu/content/wham/.

102 J. K. Yu, R. Liang, F. Liu and T. J. Martínez, *J. Am. Chem. Soc.*, 2019, **141**, 18193–18203.

103 S. Laptenok and S. R. Meech, Personal communication, 2020.

104 S. B. Nielsen, A. Lapierre, J. U. Andersen, U. V. Pedersen, S. Tomita and L. H. Andersen, *Phys. Rev. Lett.*, 2001, **87**, 228102.

105 R. S. Liu, *Acc. Chem. Res.*, 2001, **34**, 555–562.

106 W. Jarzeba, G. C. Walker, A. E. Johnson, M. A. Kahlow and P. F. Barbara, *J. Phys. Chem.*, 1988, **92**, 7039–7041.

107 D. Mandal, T. Tahara, N. M. Webber and S. R. Meech, *Chem. Phys. Lett.*, 2002, **358**, 495–501.

108 A. D. Kummer, C. Kompa, H. Niwa, T. Hirano, S. Kojima and M. E. Michel-Beyerle, *J. Phys. Chem. B*, 2002, **106**, 7554–7559.

109 K. L. Litvinenko, N. M. Webber and S. R. Meech, *J. Phys. Chem. A*, 2003, **107**, 2616–2623.

110 M. G. Romei, C. Y. Lin, I. I. Mathews and S. G. Boxer, *Science*, 2020, **367**, 76–79.